INSTITUTE OF PHYSICS PUBLISHING and INTERNATIONAL ATOMIC ENERGY AGENCY NUCLEAR FUSION

Nucl. Fusion **47** (2007) S645–S657 doi:10.1088/0029-5515/47/10/S13

Overview of recent physics results from the National Spherical Torus Experiment (NSTX)

J.E. Menard[1], M.G. Bell[1], R.E. Bell[1], S. Bernabei[1], J. Bialek[2], T. Biewer[1], W. Blanchard[1], J. Boedo[3], C.E. Bush[4], M.D. Carter[4], W. Choe[5], N.A. Crocker[6], D.S. Darrow[1], W. Davis[1], L. Delgado-Aparicio[7], S. Diem[1], C.W. Domier[8], D.A. D'Ippolito[9], J. Ferron[10], A. Field[11], J. Foley[1], E.D. Fredrickson[1], D.A. Gates[1], T. Gibney[1], R. Harvey[12], R.E. Hatcher[1], W. Heidbrink[13], K.W. Hill[1], J.C. Hosea[1], T.R. Jarboe[14], D.W. Johnson[1], R. Kaita[1], S.M. Kaye[1], C.E. Kessel[1], S. Kubota[6], H.W. Kugel[1], J. Lawson[1], B.P. LeBlanc[1], K.C. Lee[8], F.M. Levinton[15], N.C. Luhmann, Jr.[8], R. Maingi[4], R.P. Majeski[1], J. Manickam[1], D.K. Mansfield[1], R. Maqueda[15], R. Marsala[1], D. Mastrovito[1], T.K. Mau[3], E. Mazzucato[1], S.S. Medley[1], H. Meyer[11], D.R. Mikkelsen[1], D. Mueller[1], T. Munsat[16], J.R. Myra[9], B.A. Nelson[14], C. Neumeyer[1], N. Nishino[17], M. Ono[1], H.K. Park[1], W. Park[1], S.F. Paul[1], T. Peebles[6], M. Peng[4], C. Phillips[1], A. Pigarov[3], R. Pinsker[10], A. Ram[18], S. Ramakrishnan[1], R. Raman[14], D. Rasmussen[4], M. Redi[1], M. Rensink[19], G. Rewoldt[1], J. Robinson[1], P. Roney[1], A.L. Roquemore[1], E. Ruskov[13], P. Ryan[4], S.A. Sabbagh[2], H. Schneider[1], C.H. Skinner[1], D.R. Smith[1], A. Sontag[2], V. Soukhanovskii[19], T. Stevenson[1], D. Stotler[1], B.C. Stratton[1], D. Stutman[7], D. Swain[4], E. Synakowski[19], Y. Takase[20], G. Taylor[1], K. Tritz[7], A. von Halle[1], M. Wade[10], R. White[1], J. Wilgen[4], M. Williams[1], J.R. Wilson[1], H. Yuh[15], L.E. Zakharov[1], W. Zhu[2], S.J. Zweben[1], R. Akers[11], P. Beiersdorfer[19], R. Betti[21], T. Bigelow[4], M. Bitter[1], P. Bonoli[18], C. Bourdelle[22], C.S. Chang[23], J. Chrzanowski[1], L. Dudek[1], P.C. Efthimion[1], M. Finkenthal[7], E. Fredd[1], G.Y. Fu[1], A. Glasser[24], R.J. Goldston[1], N.L. Greenough[1], L.R. Grisham[1], N. Gorelenkov[1], L. Guazzotto[21], R.J. Hawryluk[1], J. Hogan[4], W. Houlberg[4], D. Humphreys[10], F. Jaeger[4], M. Kalish[1], S. Krasheninnikov[3], L.L. Lao[10], J. Lawrence[25], J. Leuer[10], D. Liu[13], G. Oliaro[1], D. Pacella[26], R. Parsells[1], M. Schaffer[10], I. Semenov[27], K.C. Shaing[28], M.A. Shapiro[18], K. Shinohara[29], P. Sichta[1], X. Tang[24], R. Vero[7], M. Walker[10] and W. Wampler[30]

[1] Princeton Plasma Physics Laboratory, Princeton University, Princeton, NJ 08543, USA
[2] Department of Applied Physics, Columbia University, NYC, NY, USA
[3] University of California, San Diego, CA, USA
[4] Oak Ridge National Laboratory, Oak Ridge, TN, USA
[5] Korea Advanced Institute of Science and Technology, Taejon, Korea
[6] University of California, Los Angeles, CA, USA
[7] Johns Hopkins University, Baltimore, MD, USA
[8] University of California, Davis, CA, USA
[9] Lodestar Research Corporation, Boulder, CO, USA
[10] General Atomics, San Diego, CA, USA
[11] Euratom-UKAEA Fusion Associates, Abingdon, Oxfordshire, UK
[12] Comp-X, Del Mar, CA, USA
[13] University of California, Irvine, CA, USA
[14] University of Washington, Seattle, WA, USA
[15] Nova Photonics, Princeton, NJ, USA
[16] University of Colorado, Boulder, CO, USA
[17] Hiroshima University, Hiroshima, Japan
[18] Massachusetts Institute of Technology, Cambridge, MA, USA
[19] Lawrence Livermore National Laboratory, Livermore, CA, USA
[20] University of Tokyo, Tokyo, Japan

0029-5515/07/100645+08$30.00 Printed in the UK

[21] University of Rochester, Rochester, NY, USA
[22] CEA, Cadarache, France
[23] New York University, NYC, NY, USA
[24] Los Alamos National Laboratory, Los Alamos, NM, USA
[25] Princeton Scientific Instruments, Princeton, NJ, USA
[26] ENEA, Frascati, Italy
[27] Kurchatov Institute, Russia
[28] University of Wisconsin, Madison, WI, USA
[29] JAERI, Naka, Japan
[30] Sandia National Laboratory, Albuquerque, NM, USA

E-mail: jmenard@pppl.gov

Received 2 January 2007, accepted for publication 28 March 2007
Published 18 September 2007
Online at stacks.iop.org/NF/47

Abstract
The National Spherical Torus Experiment (NSTX) has made considerable progress in advancing the scientific understanding of high performance long-pulse plasmas needed for future spherical torus (ST) devices and ITER. Plasma durations up to 1.6 s (five current redistribution times) have been achieved at plasma currents of 0.7 MA with non-inductive current fractions above 65% while simultaneously achieving β_T and β_N values of 17% and 5.7 (%m T MA^{-1}), respectively. A newly available motional Stark effect diagnostic has enabled validation of current-drive sources and improved the understanding of NSTX 'hybrid'-like scenarios. In MHD research, ex-vessel radial field coils have been utilized to infer and correct intrinsic EFs, provide rotation control and actively stabilize the $n = 1$ resistive wall mode at ITER-relevant low plasma rotation values. In transport and turbulence research, the low aspect ratio and a wide range of achievable β in the NSTX provide unique data for confinement scaling studies, and a new microwave scattering diagnostic is being used to investigate turbulent density fluctuations with wavenumbers extending from ion to electron gyro-scales. In energetic particle research, cyclic neutron rate drops have been associated with the destabilization of multiple large toroidal Alfven eigenmodes (TAEs) analogous to the 'sea-of-TAE' modes predicted for ITER, and three-wave coupling processes have been observed for the first time. In boundary physics research, advanced shape control has enabled studies of the role of magnetic balance in H-mode access and edge localized mode stability. Peak divertor heat flux has been reduced by a factor of 5 using an H-mode-compatible radiative divertor, and lithium conditioning has demonstrated particle pumping and results in improved thermal confinement. Finally, non-solenoidal plasma start-up experiments have achieved plasma currents of 160 kA on closed magnetic flux surfaces utilizing coaxial helicity injection.

PACS numbers: 52.55.Fa, 52.55.Wq, 52.55.Tn, 52.25.Fi, 52.55.Rk, 52.55.Pi

1. Progress in plasma performance and understanding

The National Spherical Torus Experiment (NSTX) [1, 2] has made considerable progress in advancing the scientific understanding of high performance long-pulse plasmas needed for low aspect ratio ST [3] concepts and for ITER. Several new tools [4] have aided this progress including modified divertor poloidal field (PFs) coils for combined high triangularity and high elongation [5], a motional Stark effect diagnostic operable at low magnetic field strength [6] and six midplane ex-vessel coils producing controllable radial magnetic field perturbations for rotation control [7], error field (EF) correction [4] and resistive wall mode (RWM) control at ITER-relevant low plasma rotation values [8].

As shown in figure 1(*a*), plasma flat-top durations approaching five current redistribution times [9] and 50 energy confinement times have been achieved with the product of normalized beta and confinement enhancement, $\beta_N H_{89P}$, in the range needed for an ST-based component test facility (CTF) [10]. The longest discharge pulse length achieved to date using up to 7 MW of neutral beam injection (NBI) heating is 1.6 s—a 60% increase relative to 2004. These discharges have flat-top plasma currents of 0.7 MA with peak non-inductive (NI) current fractions $f_{NI} \leqslant 65\%$ while simultaneously achieving $\beta_T \leqslant 17\%$ and $\beta_N \leqslant 5.7$(%m T MA^{-1}), respectively [11]. This performance has been achieved by operating with increased boundary triangularity at high elongation utilizing advanced shape control [12], from a reduction in the severity of edge-localized modes (ELMs) at high elongation by operating with slightly negative magnetic balance [5, 13] and by operation above the ideal no-wall stability limit and near the ideal-wall stability limit [14–16] via rotational stabilization of the RWM. NSTX now routinely operates with sustained boundary elongation of 2.4–2.5, and as is evident from figure 1(*b*), can stably access significantly higher elongation with a peak value of 3 achieved in 2006 [17]. Since $f_{BS} \propto \sqrt{\epsilon}(1+\kappa^2)\beta_N^2/\beta_T$, increased elongation is a primary means of increasing the bootstrap (BS) fraction while maintaining high β_T. As seen in

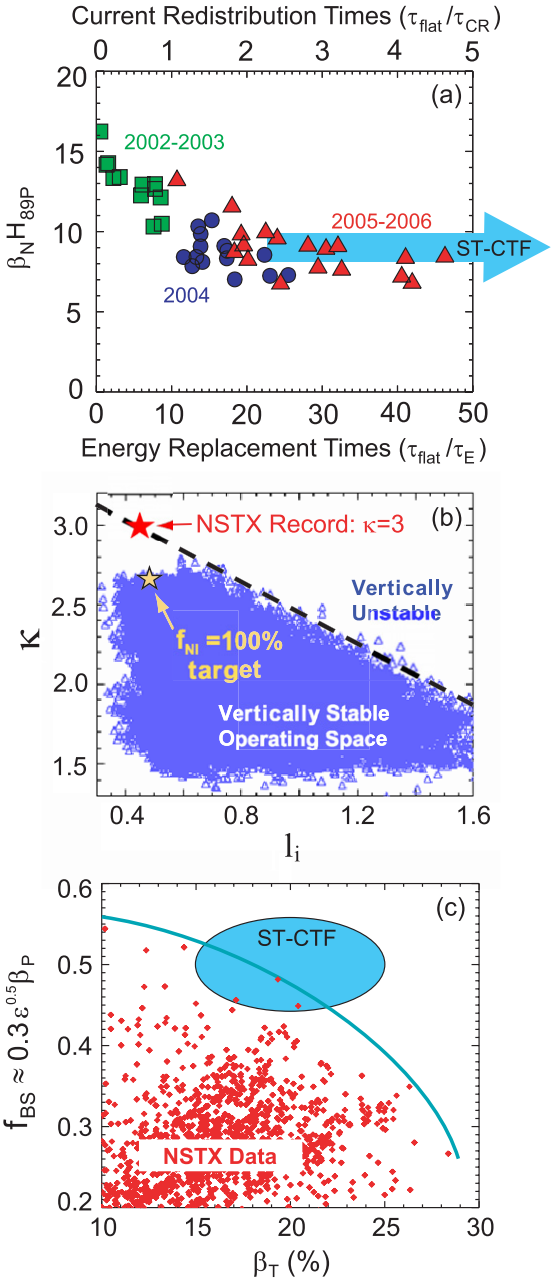

Figure 1. (*a*) Product of normalized beta β_N and H-mode confinement enhancement factor H_{89P} versus pulse length normalized to energy confinement time τ_E (bottom axis) and current redistribution time τ_{CR} (top axis), (*b*) peak elongation κ versus internal inductance l_i and (*c*) peak estimated bootstrap fraction f_{BS} versus toroidal beta β_T.

figure 1(*c*), the highest performance NSTX plasmas are very close to simultaneously achieving $\beta_T = 20\%$ and $f_{BS} = 50\%$ projected to be required for a ST-CTF.

The longest duration discharges of the NSTX described above often maintain central q above unity for many current redistribution times. An improved understanding of this physics may offer insight into mechanisms that sustain the 'hybrid' scenario proposed as a possible improved high-Q scenario for the ITER [18]. Such studies have been enabled by a 12 channel MSE diagnostic operable at the low toroidal fields (TFs) of the NSTX [6].

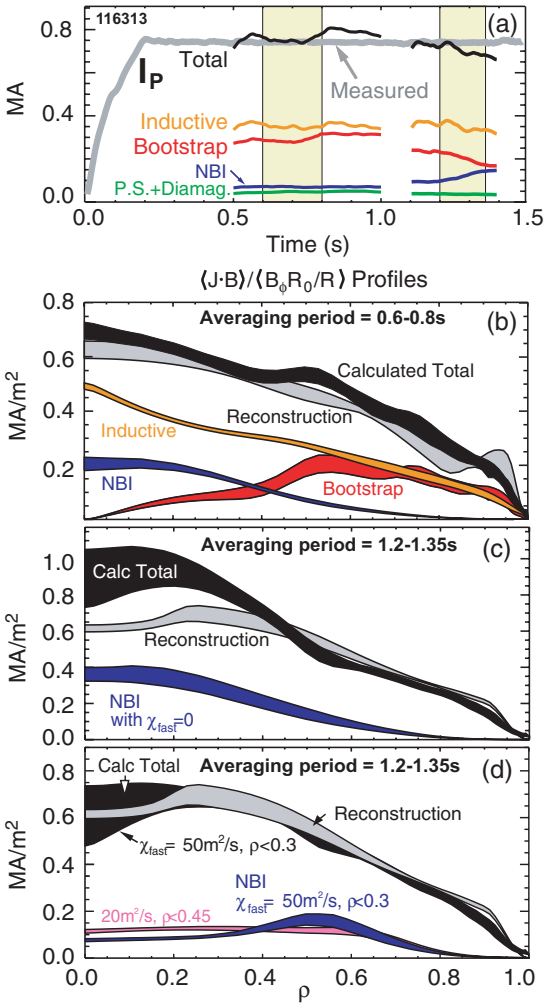

Figure 2. (*a*) Comparison of measured (grey) and calculated (black) total plasma current with calculated inductive and NI contributions also shown, (*b*) comparison of reconstructed and calculated current density profiles during a high β and MHD-quiescent phase ($t = 0.6$–0.8 s) and comparison of reconstructed and calculated current density profiles during saturated $n = 1$ core interchange mode activity ($t = 1.2$–1.35 s) without (*c*) and with (*d*) AFID included in the TRANSP calculation of the beam-driven current.

Figure 2(*a*) compares the measured total plasma current with the calculated current from both inductive and NI sources. Here, the loop voltage profiles are computed directly from the MSE-constrained reconstructions, the inductive and BS currents are calculated using Sauter's formulae [19] and the NBI current drive (NBICD) is computed using TRANSP [20]. For discharges that are sufficiently MHD-quiescent, the measured and calculated total currents and neutron rates typically agree to within 5–10%. As seen in figure 2(*b*), the reconstructed and calculated plasma current density profiles are also in good agreement with the NBICD dominating the NI current drive in the plasma core and BS current dominating off-axis. During the highest $\beta_N = 5.5$–6 phase of such discharges, the plasma is typically near the ideal-wall limit, and repeated excursions above this limit have been observed to trigger saturated core-localized $n = 1$ interchange-type instabilities [11]. During such MHD activity, discrepancies between the reconstructed and the calculated

core current density as large as 40% have been observed as shown in figure 2(*c*). Significant deviations between the predicted and the measured fast-particle distributions are also evident in the neutron rate and neutral particle analyzer (NPA) data [21]. Agreement between measurement and prediction is significantly improved if the $n = 1$ mode is assumed to cause significant NBI fast-particle redistribution in the plasma core with moderate global loss <15%. As seen in figure 2(*d*), consistency between the reconstructed and the calculated total current density profiles can be obtained if MHD-induced diffusion of the NBI fast ions ($\chi_{\rm fast} = 20$–$50\,{\rm m}^2\,{\rm s}^{-1}$) is assumed in the TRANSP calculation of the beam-driven current. Such fast-ion redistribution can apparently convert a centrally peaked NBICD profile into a flat or even hollow profile. More details of the modelling of the fast-ion redistribution for this discharge are provided in [11]. For a discharge similar to that shown in figure 2 but with earlier $n = 1$ mode onset near $t = 0.6$ s, figure 3 shows the (*a*) time-dependent profiles and (*b*) energy dependence of the anomalous fast-ion diffusion (AFID) needed to match (*c*) the energy distribution as measured by NPA and (*d*) the neutron rate in the presence of the MHD activity. As shown in figure 3(*b*), a comparatively lower level of AFID is also invoked prior to the onset of MHD activity at $t = 0.6$ s in order to account for apparent fast-ion redistribution by TAE activity. With this AFID model included, the reconstructed core current density profile is in much better agreement with the prediction [21], again consistent with MHD activity redistributing the NBI-driven current. The detailed mechanisms by which the TAE and MHD instabilities cause such fast-ion redistribution are under active investigation.

Validation of NI current-drive sources in the absence of large-scale MHD activity has also enabled identification of fully NI scenarios extrapolated from present discharge parameters as shown in figure 2 [22]. Fully NI $I_{\rm P} = 700$ kA, $B_{\rm T} = 5.2$ kG scenarios are calculated to be achievable by increasing the thermal temperatures 50–70%, decreasing the electron density 25% and increasing elongation from 2.3 to 2.6 and bottom triangularity from 0.75 to 0.85. Self-consistent profiles for such a scenario are shown in figure 4. The necessary increase in $\beta_{\rm N}$ from 5.6 to 6.7 would require either enhanced confinement from lithium wall conditioning as described in section 5 and/or efficiently coupled high-harmonic fast-wave (HHFW) heating as described in section 6. This increased $\beta_{\rm N}$ scenario is calculated to be $n = 1$–3 ideal-wall stable for the predicted increase in $q_{\rm min}$ to 2.4 from 1.3 and would require RWM stabilization either from plasma rotation and dissipation and/or active feedback control.

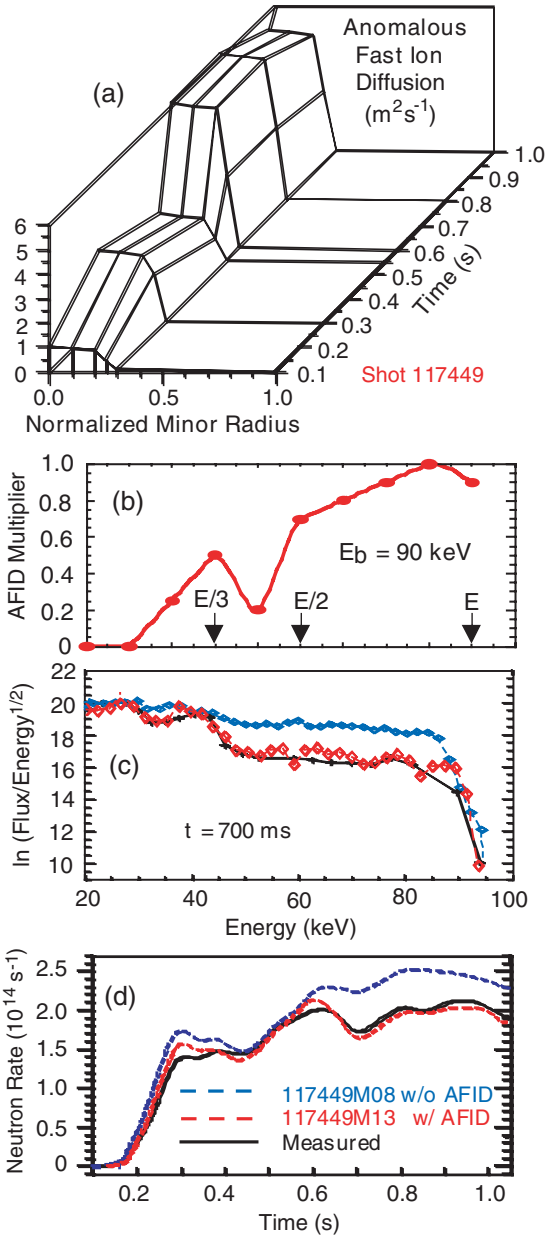

Figure 3. (*a*) Time-dependent profile of AFID used to simulate fast-ion redistribution by low-frequency MHD activity for a discharge similar to that shown in figure 2, (*b*) energy dependence of the AFID model, (*c*) improved agreement with measured NPA energy spectrum with AFID model included and (*d*) comparison of the measured and simulated neutron rates with and without AFID.

2. Macroscopic stability

In most high-$\beta_{\rm N}$ scenarios in the NSTX operating above the no-wall stability limit, RWM stabilization is achieved passively from high plasma rotation due to unidirectional tangential NBI heating. However, some discharge scenarios exhibit rotation slow-down at radii near the $q = 2$ and 3 surfaces and suffer rapid collapses in β. Six midplane ex-vessel coils (RWM/EF coils) producing controllable $n = 1$ and/or $n = 3$ radial magnetic fields have been commissioned on the NSTX and utilized to study EF and RWM physics in detail. Real-time measurement and closed-loop feedback control of low-frequency MHD activity including unstable RWMs and EFs amplified by the stable RWM have also been implemented on the NSTX.

Low-density locked-mode threshold experiments have identified $n = 1$ resonant EFs of 1–3 G [4] calculated at the $q = 2$ surface near $\rho_{\rm pol} \equiv \sqrt{\hat{\psi}_{\rm pol}} = 0.7$–$0.8$. After subtracting the inferred intrinsic EF from the total applied field at locking, the density dependence of the 2/1 locked-mode threshold scales as $\bar{n}_{\rm e}^{0.93}$ as shown in figure 5(*a*) for $I_{\rm P} = 700$ kA, $B_{\rm T} = 0.45$ T lower single null discharges. This

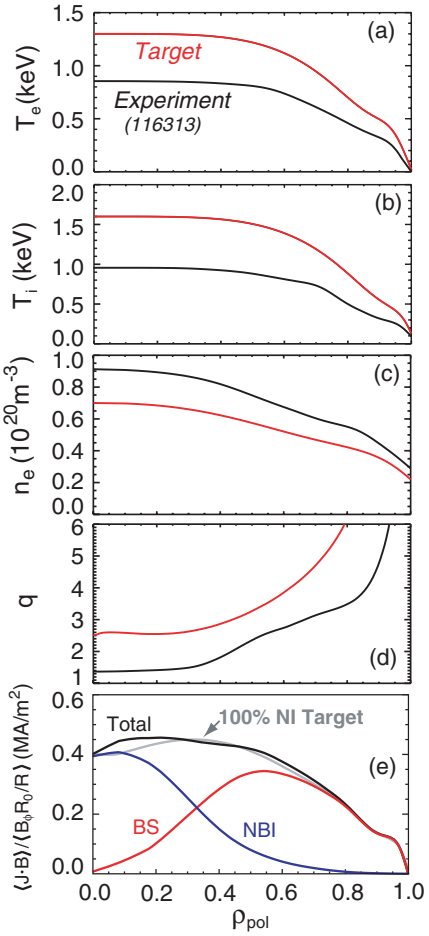

Figure 4. Present experimental profiles (black) and profiles needed (red) to achieve a fully NI target equilibrium utilizing only NBI and BS current. (*a*) Electron temperature, (*b*) ion temperature, (*c*) electron density, (*d*) safety factor profile and (*e*) parallel current density profiles (for the fully non-inductive target equilibrium).

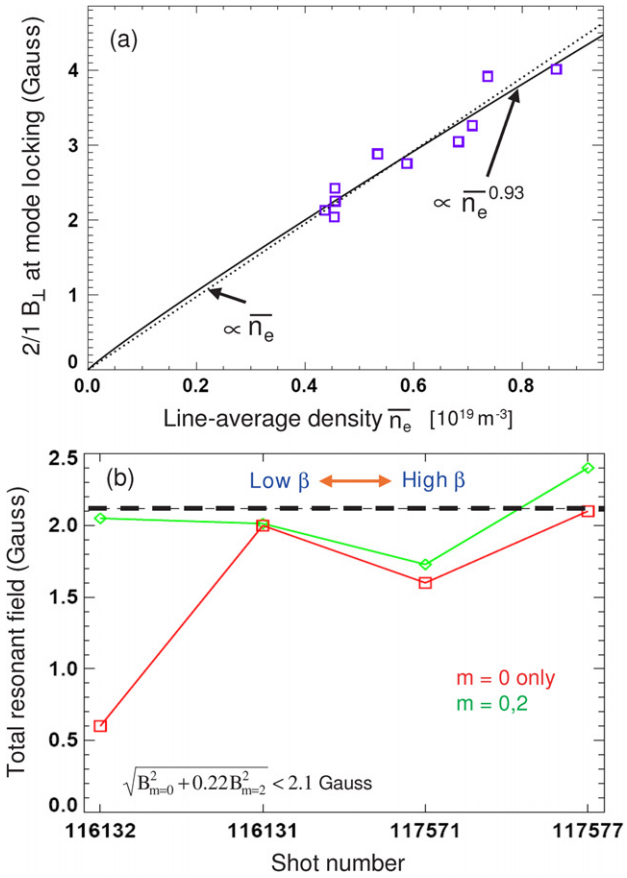

Figure 5. (*a*) Density scaling of the 2/1 component of the flux-surface-normal B-field amplitude at locked-mode onset versus line-average density and (*b*) total (intrinsic+applied) EF threshold calculated at the $q = 3$ surface at the onset of locking (low β) and rotation collapse (high β).

threshold scaling is very nearly linear in density consistent with theory expectations and results from higher aspect ratio tokamaks [23, 24].

Additional experiments at higher β revealed EFs of similar magnitudes but of opposite polarity. The source of this EF has since been traced to the motion of the TF central conductor bundle relative to the vacuum vessel and PF coils. The EF is measured to be proportional to the time-delayed and partially rectified product of the OH and TF coil currents, implying a non-axisymmetric magnetic interaction between the OH and TF coils. The change in EF polarity is therefore attributed to the change in polarity of the double-swing OH transformer current after the current passes through zero. Using the improved understanding of the intrinsic EF source, the low and high β locking data together also revealed that minimizing the 2/1 component of the vacuum EF at the computed 2/1 surface inside the plasma does not give optimal correction, i.e. the minimization of flow damping. The $m = 0$ component of the vacuum EF is found to be significant for the TF shift, and this component also has a polarity opposite to the other $|m| > 0$ components. As shown in figure 5(*b*), balancing the $m = 0$ against the $m = 2$ component can empirically provide a nearly invariant threshold field of $\approx$2 G for both data sets when the fields are added in quadrature. This result may imply that the non-resonant $m = 0$ component of the flow damping is very important [25] or that the ideal plasma response to the EF is much different than the vacuum response.

Correction of this EF has been attempted using several control methods. First, as seen in figure 6, correction of the OH×TF EF (black curves) utilizing a real-time estimate of the TF coil motion increases the pulse duration above the no-wall limit by approximately 50% relative to no correction (red curves) during the high β_N phase. As seen in the same figure, the addition (green curves) of gain and phase-optimized closed-loop feedback control of the measured in-vessel $n = 1$ PF to OH×TF correction can double the duration above the no-wall limit. Additional tests in these discharges find that closed-loop $n = 1$ feedback alone does not provide robust pulse extension early in the high-β_N phase and that the OH×TF correction is not yet optimized late in the high-β_N phase. Finally, using the time-average of the OH×TF plus closed-loop $n = 1$ feedback coil currents (blue curves) provides nearly identical performance as the non-averaged coil currents. Because the measured RWM growth time (see below) is much shorter than the averaging time used in these experiments, this result implies that the feedback control system responds to plasma induced EF amplification and aids in sustaining the plasma rotation which stabilizes the RWM, rather than feeding back directly

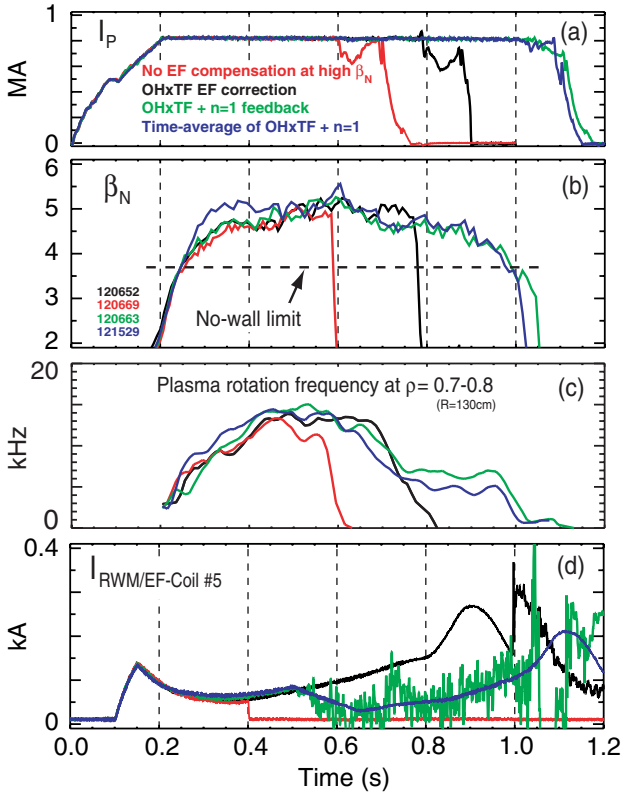

Figure 6. (*a*) Plasma current, (*b*) normalized beta, (*c*) plasma rotation near $q = 2$ and three surfaces and (*d*) RWM/EF coil current during dynamic EF correction experiments.

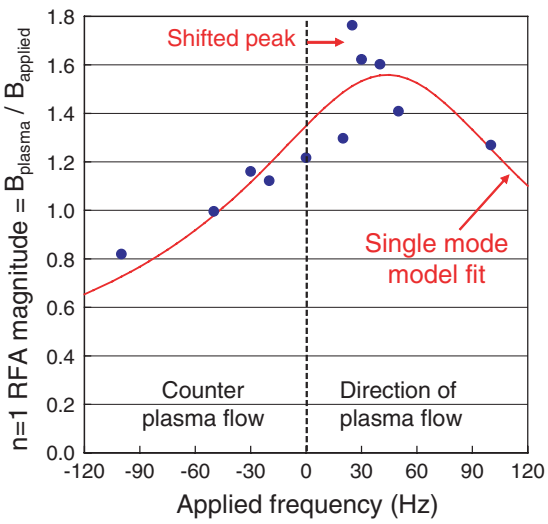

Figure 7. Resonant field amplification (RFA) versus applied frequency of $n = 1$ travelling waves excited using the midplane mode-control coils of the NSTX in a plasma operating above the $n = 1$ no-wall stability limit.

on the unstable RWM. Similar results have also been obtained on DIII-D [26]. Further, these results are consistent with low-frequency MHD spectroscopy measurements [27] indicating the presence of a stable $n = 1$ RWM resonant at 30–50 Hz in the co-rotation direction [28] as shown in figure 7.

The same RWM/EF control coils used for EF correction studies have also been used to investigate magnetic braking

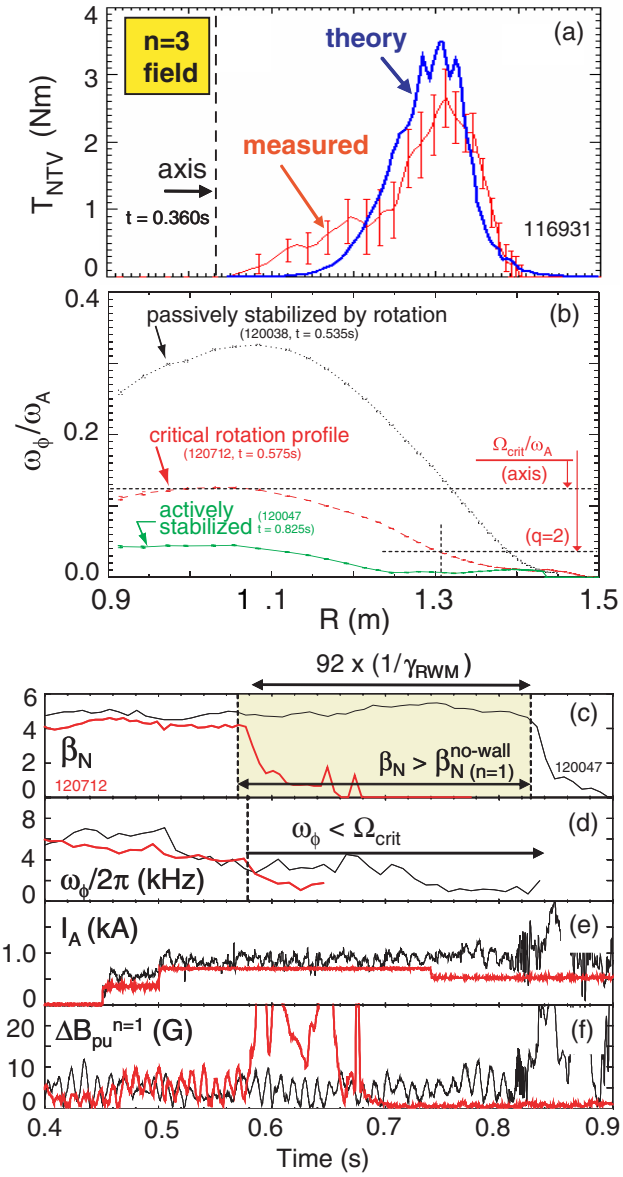

Figure 8. (*a*) Torque comparison, (*b*) plasma rotation profiles and evolution of (*c*) normalized beta, (*d*) rotation, (*e*) RWM/EF coil current and (*f*) mode $n = 1$ PF for magnetic braking and RWM feedback experiments.

physics and feedback stabilization of the RWM. Rotation damping from both $n = 1$ and $n = 3$ fields has been compared with neoclassical toroidal viscosity (NTV) theory. Figure 8(*a*) shows an example of the good agreement between the measured and the predicted torques for $n = 3$ radial magnetic fields applied by the RWM/EF coils [7]. Both $n = 1$ and $n = 3$ applied fields have been shown capable of lowering the plasma rotation to values below the RWM critical rotation frequency. However, the non-resonant $n = 3$ field is most commonly used for magnetic braking when studying the $n = 1$ RWM to minimize complications in measuring and interpreting the $n = 1$ RWM growth. This technique has been used to measure the $n = 1$ critical rotation frequency [15, 28] and has allowed controlled experiments on $n = 1$ RWM feedback stabilization at ITER-relevant low plasma rotation levels [8].

The black curve in figure 8(*b*) illustrates the undamped rotation profile typical of the rotationally stabilized plasmas in these experiments, while the red and green curves show the rotation profiles at $n = 1$ RWM marginal stability and during RWM closed-loop feedback control, respectively. As seen in the figure, the rotation during feedback is approximately 1/3 of the critical value and is below the normalized rotation value predicted for ITER. Figures 8(*c*) and (*d*) show that feedback control of the RWM (black curves) can extend the duration of high β_N above the no-wall limit by over 90 RWM growth times while the plasma rotation is maintained below the experimentally determined critical rotation frequency. This low rotation is sustained by steady $n = 3$ braking from the nearly constant RWM/EF coil currents as illustrated in figure 8(*e*). Finally, figure 8(*f*) shows the $n = 1$ mode PF as measured by the in-vessel RWM/EF sensor array with (black) and without (red) close-loop RWM control enabled demonstrating the suppression of RWM $n = 1$ field by the feedback system. The above results improve the prospects for robust EF and RWM control at high β_N in ITER and other magnetic fusion concepts operating above the no-wall ideal-stability limit.

3. Transport and turbulence

The low aspect ratio and wide range of β values accessible in NSTX (β_T up to 40%) provide unique data for understanding the dependence of energy confinement on these parameters for the ST and for ITER. Initial H-mode energy confinement scaling studies for NSTX found a weaker dependence on plasma current than at a conventional aspect ratio and a stronger dependence on B_T [29]. NSTX H-mode confinement data have also been incorporated into international confinement databases, and resulting scalings using this and the higher aspect ratio data indicate a stronger positive inverse aspect ratio dependence and weaker β dependence than in the commonly used ITER98PB(y,2) scaling. More recent experiments have elucidated the distinct roles of ion and electron thermal transport in the global energy confinement scaling [30]. In particular, increasing the toroidal magnetic field from 0.35 to 0.55 T results in a broadening of the electron temperature profile and a reduction in χ_e in the outer half of the plasma minor radius. Interestingly, the central electron temperature is observed to increase only by 10–20% during this scan. As the plasma current is increased from 0.7 to 1.0 MA, the ion transport is reduced in the outer half of the plasma minor radius consistent with $\chi_i \approx \chi_{i\text{-neoclassical}}$. Thus, the electron transport largely determines the TF scaling, while the ion (neoclassical) transport largely determines the plasma current scaling [30].

To investigate possible causes of anomalous electron transport in the NSTX, a 1 mm microwave scattering diagnostic capable of measuring electron gyro-radius-scale turbulence has been implemented on the NSTX. Figure 9(*a*) shows a top-down view of the microwave ray paths for scattered rays accepted by the collection waveguides of the system. The 280 GHz system provides high radial spatial resolution <6 cm, high k resolution <1 cm^{-1}, the ability to scan radially from near the magnetic axis to near the edge, and measures predominantly k_r from 2 to 24 cm^{-1} covering ion to electron-scale turbulence. Data from this diagnostic will provide strong tests of anomalous

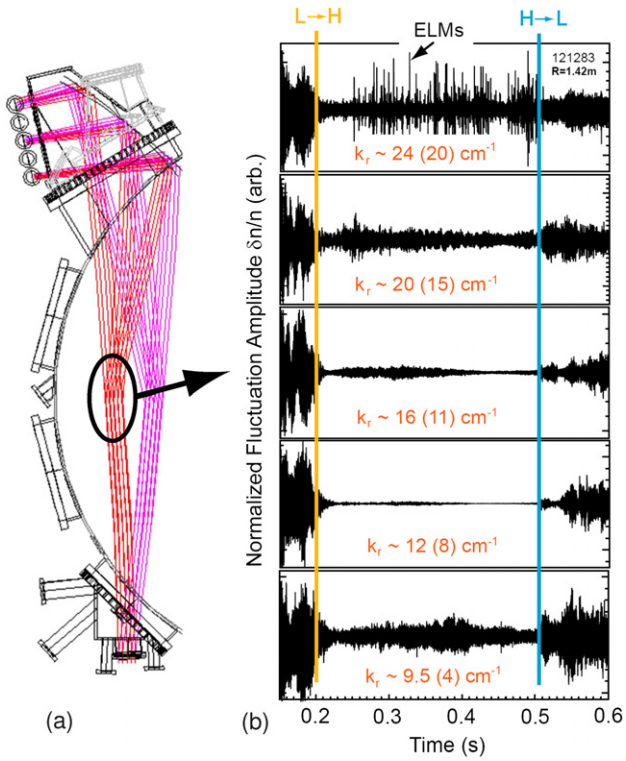

Figure 9. (*a*) Radially scannable high-k scattering diagnostic as viewed from above, (*b*) $\delta n/n$ fluctuation levels (renormalized to initial L-mode values) in the L-mode and the H-mode of a $P_{NBI} = 2$ MW, $I_P = 0.8$ MA, $B_T = 0.45$ T discharge for a range of radial wavenumbers. Wavenumbers before parentheses are for the H-mode phase, while numbers in parentheses are for the L-mode phase.

electron energy transport theories—of particular importance to developing a first-principles predictive capability for electron energy transport for the ITER and magnetic confinement devices in general. The availability of MSE data has also improved the understanding of the role of magnetic shear in energy transport. In particular, reversed magnetic shear has been demonstrated to allow the formation of electron energy transport barriers in L-mode discharges, and electron energy confinement improvement correlates with the degree of measured magnetic shear reversal [2, 4, 30].

These high-$T_e \leqslant 2$ keV L-mode discharges are typically heated with one NBI source ($P_{NBI} = 1.6$–2 MW) and achieve some of the highest transient energy confinement times in the NSTX of $\tau_E = 80$–100 ms but have low β_N limits $\leqslant 4$ and low NI current fractions relative to the positive shear $T_e \leqslant 1.2$ keV H-mode discharges heated with 4–7 MW as described in section 1. Analysis of high-k density fluctuation amplitude as a function of core magnetic shear in high-T_e L-mode discharges does indicate some dependence on magnetic shear, but firm conclusions cannot yet be drawn. However, other discharge scenarios do show clear correlations between reduced transport and reduced density fluctuation amplitudes. With the high-k system viewing at large major radius (see black oval in figure 9(*a*)), figure 9(*b*) shows a large reduction in fluctuation levels after the transition from the L-mode to the H-mode for nearly all radial wavenumbers measurable by the system. In this figure, the fluctuation amplitudes

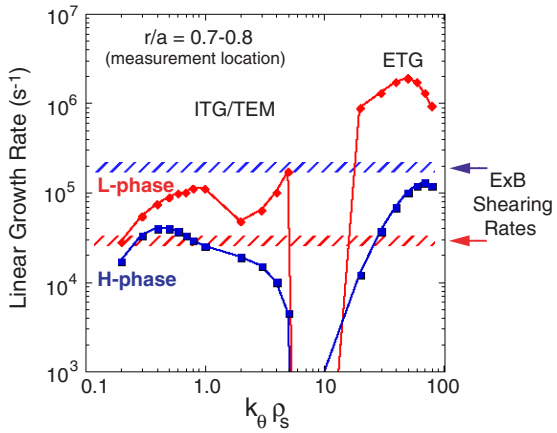

Figure 10. Linear growth rates of ITG/TEM ($k_\theta \rho_s < 10$) and ETG ($k_\theta \rho_s > 10$) micro-instabilities versus normalized poloidal wavenumber calculated with the GS2 gyro-kinetic code for the early L-mode (red) and H-mode (blue) phases of the discharge shown in figure 9. The $E \times B$ shearing rates for the H-mode and L-mode discharge phases are also shown for comparison with the linear growth rates.

at different wavenumbers should not be directly compared since the fluctuation amplitude for each channel has been renormalized to the initial L-mode amplitude for that channel.

Figure 10 shows linear micro-instability growth-rate calculations from the GS2 code [31] for plasma parameters at the radial position circled in figure 9(*a*) for the discharge shown in figure 9(*b*) during the L-mode and the H-mode phases. As seen in figure 10, ITG/TEM and ETG modes are unstable but have reduced growth rates after the transition from the L-mode to the H-mode. This decrease is consistent with the observed decrease in fluctuation levels for nearly all measured wavenumbers. During the H-mode phase, the $E \times B$ shearing rate exceeds the linear growth rate of the low-k_θ turbulence, non-linear simulations find that low-k_θ turbulence in the ITG/TEM range is suppressed and, consistent with this, the measured ion thermal diffusivity is at the neoclassical level [30]. Interestingly, as is evident in figure 9(*b*), unlike the lower-k data, the highest $k_r = 24\,\mathrm{cm}^{-1}$ signal exhibits amplitude bursts during the H-mode which correlate with ELM events. Present studies are attempting to determine if these bursts correspond directly to ELM-induced density perturbations of short radial scale-length or are instead due to beam refraction effects.

Beyond the passive observation of transport properties, lithium-pellet-induced edge temperature perturbations have allowed the core electron transport response to be probed, and the two kinds of discharges described above exhibit very different transport responses. Figure 11(*a*) shows the electron temperature evolution in a positive shear H-mode discharge ($P_{\mathrm{NBI}} = 5.5\,\mathrm{MW}$, $I_\mathrm{P} = 0.7\,\mathrm{MA}$, $B_\mathrm{T} = 0.45\,\mathrm{T}$) using two-colour ultra-soft x-ray (USXR) tomography [32]. Following the pellet perturbation, the core electron temperature gradient scale-length shown in figure 11(*b*) is essentially constant indicating very stiff profiles consistent with the existence of a critical temperature gradient. In contrast, figure 11(*c*) shows that the core electron temperature actually increases in the L-mode ($P_{\mathrm{NBI}} = 2\,\mathrm{MW}$, $I_\mathrm{P} = 1\,\mathrm{MA}$, $B_\mathrm{T} = 0.45\,\mathrm{T}$) after pellet injection, and figure 11(*d*) indicates a

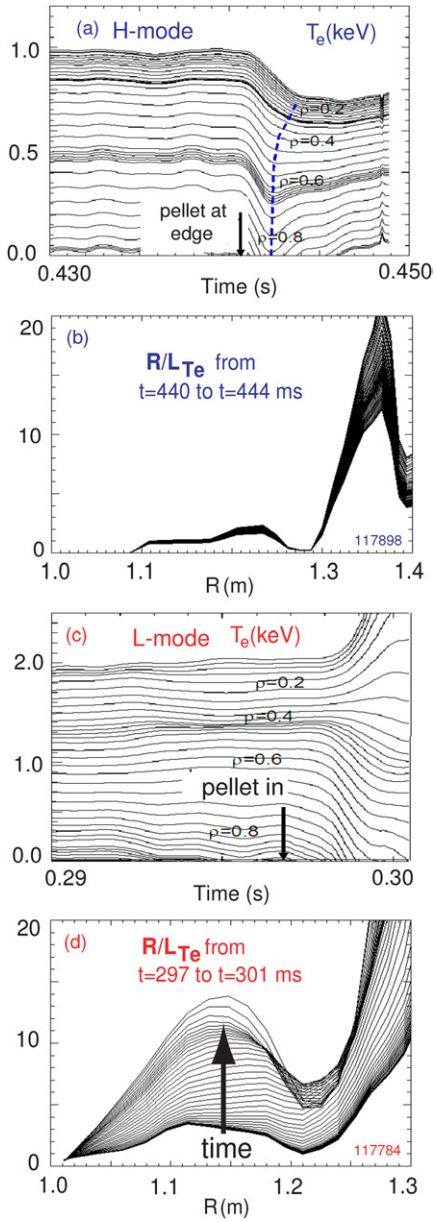

Figure 11. (*a*) T_e and (*b*) T_e gradient evolution in the H-mode and (*c*) T_e and (*d*) T_e gradient evolution in the L-mode during edge perturbations induced by lithium pellet injection.

significant increase in the normalized temperature gradient and an apparent lack of profile stiffness. The ability to create and diagnose scenarios with large variations in electron transport while largely suppressing ion turbulence makes the NSTX particularly well suited for studying electron transport physics.

4. Energetic particle physics

The NSTX is also well suited to investigating fast-ion driven instabilities and their influence on fast-particle confinement for both ITER and STs. NBI-heated NSTX plasmas can match and exceed the fast-ion β and velocity ratio $v_{\mathrm{fast}}/v_{\mathrm{Alfven}}$ of ITER (albeit at much higher fast-ion ρ_*) with complete diagnostic coverage including MSE. Cyclic neutron rate drops have been associated with the destabilization of

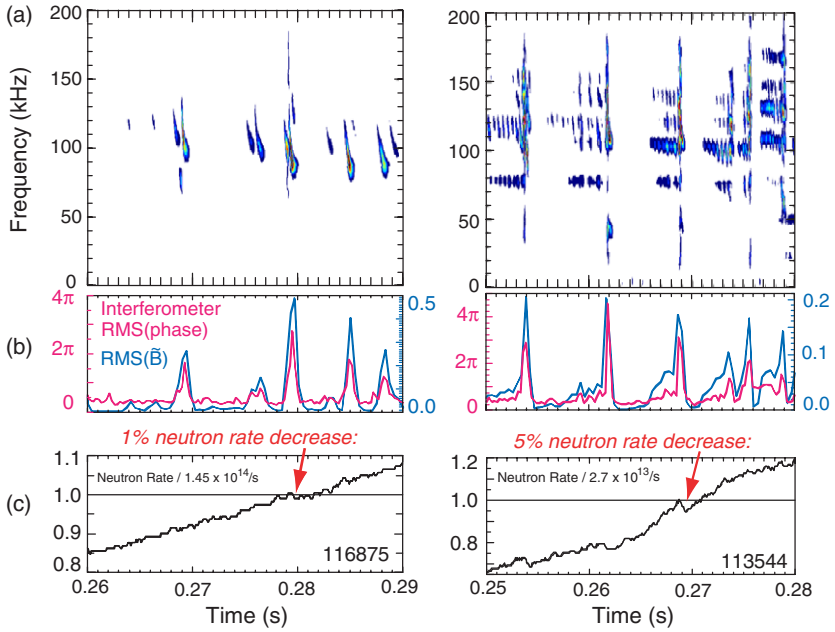

Figure 12. (*a*) Mode frequency spectra, (*b*) density fluctuation and Mirnov oscillation amplitudes and (*c*) neutron rate decrements during single-mode TAE (left) and multi-mode TAE (right) bursts.

multiple large TAEs analogous to the 'sea-of-TAEs' predicted for ITER, albeit at the lower TAE toroidal mode number $n = 1$–6 [33]. NPA data show that the strongest particle density modulation occurs below the injection half-energy and that the density of the highest energy ions is modulated by roughly 10% [21]. Figure 12 compares the mode frequencies, fluctuation amplitudes and neutron rate decrements (arising from fast-ion loss and/or redistribution) during single-mode and multi-mode TAE burst events. An important finding evident in this figure is that multi-mode burst events lead to 5× larger neutron rate decrements than single-mode events despite having 2–3× lower RMS B-field fluctuation amplitude (0.15–0.2 G versus 0.3–0.5 G). During the larger neutron rate decrement events, decreases in plasma stored energy and increases in edge D-alpha light emission are also measured—consistent with some fraction of fast ions being lost from the plasma. These data imply that the structure and multiplicity of TAE modes is just as important as mode amplitude (if not more so) in determining the mode-induced fast ion transport. Interestingly, recent NSTX results indicate that multi-mode coupling is not constrained to a single class of fast-ion instability. Figure 13(*a*) shows that TAE modes can coexist with energetic particle modes (EPMs), and bi-coherence analysis indicates that an $n = 1$ EPM mode can couple to two higher-n (and higher frequency) TAE modes through a three-wave coupling process [34]. In fact, the dominant EPM can drive the TAE amplitude envelope to be toroidally localized during mode propagation as shown in figure 13(*b*). In figures 13(*a*) and (*b*), $\delta\phi$ is the relative phase between launched and reflected fixed-frequency ($f = 50$ GHz) microwaves which reflect from a cutoff layer corresponding to an electron density $n_e \approx 3 \times 10^{19} \mathrm{m}^{-3}$ at a minor radius $r/a \approx 0.4$. The data in figures 12 and 13 together imply that the structure, multiplicity and non-linear coupling characteristics of multiple fast-ion instabilities could all play a role in determining fast-ion transport in future ST devices and ITER.

5. Boundary physics

Improved understanding and control of both steady-state and transient heat fluxes to the divertor and other plasma facing components (PFCs) are essential for the successful operation of ITER and future ST devices such as an ST-CTF. Large transient heat loads from ELMs pose a serious risk to the divertor of next-step devices, and this has motivated research on developing small ELM regimes and complete ELM suppression using 'edge-ergodization' coils [35]. Modest changes in ELM size and frequency have been achieved in NSTX using the RWM/EF coils, and additional analysis indicates that such edge ergodization can be further optimized [36]. However, a small 'Type V' ELM regime with $\Delta W / W_{TOT} < 1\%$ has been discovered on the NSTX [37], and accessibility to this regime has been characterized as a function of pedestal collisionality, β_N, and boundary shaping [38]. More recent studies indicate that access to this small ELM regime may be possible at low pedestal collisionality at the high boundary shaping factors accessible in the ST, and more detailed measurements of Type V ELM structure and dynamics have been obtained [13]. ELM severity is also observed to be very sensitive to magnetic balance, i.e. proximity to a double-null boundary shape. Optimal ELM characteristics are typically obtained in a shape with negative bias, i.e. towards lower single null [5, 13]. Studies of these effects have been facilitated by the successful implementation of rt-EFIT and the precise boundary control it enables [12]. This shape control capability has also been exploited to enable similarity experiments with MAST and DIII-D investigating the dependence of the H-mode pedestal structure on the aspect ratio. In these experiments, the boundary shape and electron collisionality (ν_e^*) and normalized ion gyro-radius (ρ_i^*) at the top of the outboard pedestal are matched. The pedestal data from all three devices is presently being assessed to develop an improved understanding for

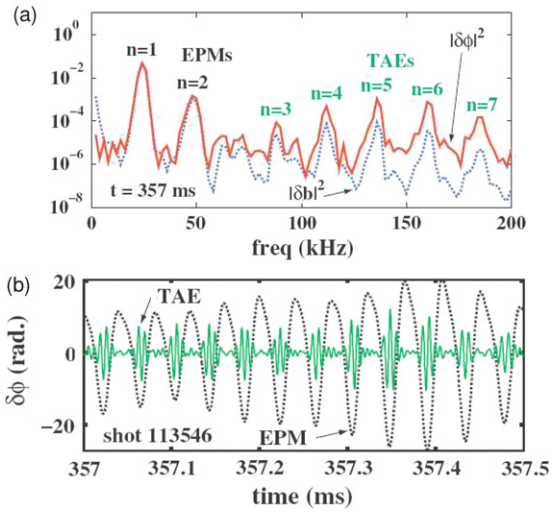

Figure 13. (*a*) Frequency spectrogram of Mirnov δb and 50 GHz microwave reflectometer phase perturbation $\delta\phi$ showing multiple EPM and TAE modes and (*b*) total reflectometer phase perturbations from EPMs and TAEs. The toroidally localized TAE amplitude envelope, caused by three-wave interactions with the EPMs, is seen as a pulse of oscillations each time it propagates past the reflectometer.

reliably extrapolating from present experiments to the pedestal parameters expected in ITER [39].

Outside the pedestal, particle and energy transport in the scrape-off-layer (SOL) are also being actively investigated both theoretically and experimentally. In particular, a two-region model has been developed to study the effects of magnetic geometry and collisionality on edge turbulence and propagation of filamentary coherent structures (blobs) [40]. Figure 14(*a*) shows [41] reasonable agreement between the 'blob' normalized velocity and size inferred from gas-puff-imaging data and the bounds predicted by the two-region theory. In this figure, the normalized blob size $\hat{a}$ is defined as the ratio of the blob size a_b to a scale-length $a_* \equiv L_{||}^{2/5}\rho_s^{4/5}/R^{1/5}$ arising from a competition between cross-field ion polarization current and sheath end-loss current. Here $L_{||}$ is the blob parallel connection length, $\rho_s = c_s/\Omega_i$ is the sound-speed ion Larmor radius and R is the tokamak major radius. The blob normalized radial velocity $\hat{v}$ is defined as the ratio of the blob radial velocity v_r to $v_* \equiv c_s\sqrt{a_*/R}$. The NSTX edge reciprocating probe also measures the density fluctuations associated with the filamentary coherent structures [42]. As seen in figure 14(*b*), the probe is located on the outboard side of the plasma below the vertical midplane and can probe several centimetres inside the separatrix. As shown in figures 14(*c*)–(*e*), far inside the separatrix, density holes (negative spikes on I_{sat}) are commonly measured, a mixture of density holes and peaks is measured just inside the separatrix and only density peaks are found in the SOL. The correlation between density holes inside the plasma with density peaks in the SOL is an active area of experimental and theoretical study.

High steady-state heat flux levels also pose serious issues for future STs and ITER. In NSTX, reductions in peak divertor heat flux have been achieved using both detached and radiative divertor scenarios via gas puffing at the inner strike point and/or private flux region in lower single null discharges [43]. The

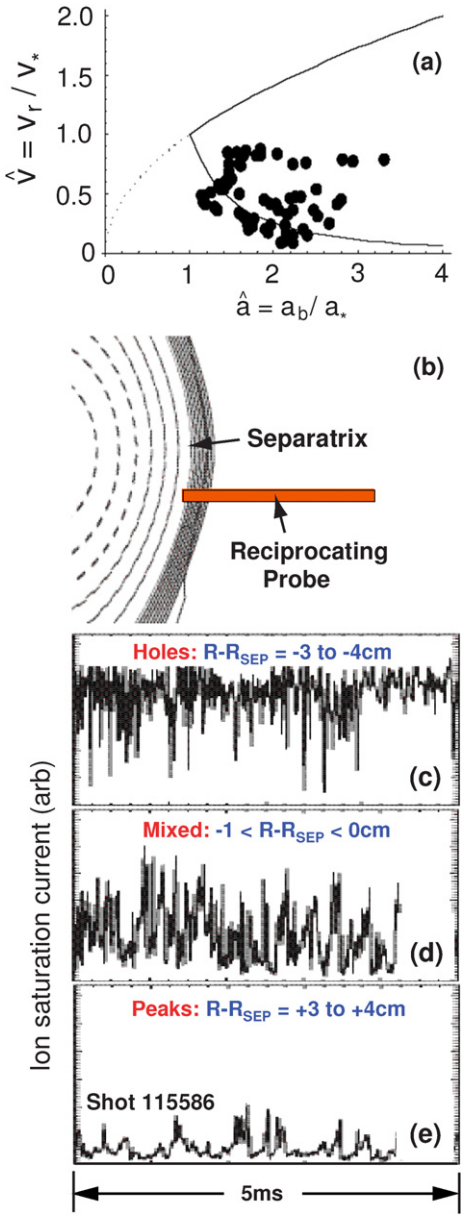

Figure 14. (*a*) Measured (circles) 'blob' normalized radial velocity versus normalized radial scale-size compared with predicted bounds (lines), (*b*) edge reciprocating probe position relative to plasma boundary, (*c*) ion saturation current fluctuations far inside the separatrix, (*d*) just inside the separatrix and (*c*) outside the separatrix in the scrape-off-layer (SOL).

inner strike point of the NSTX divertor discharges is typically observed to be fully detached, while the outer strike point is attached [44]. With sufficient D_2 gas injection in the divertor, it is also possible to partially detach the outer strike point, but thus far this has led to deleterious MHD activity and loss of the H-mode. However, with reduced gas input, a 'radiative divertor' regime has been developed which also produces significant reductions in peak divertor heat flux. Figures 15(*a*) and (*b*) show that the required gas injection in the divertor has no apparent impact on H-mode confinement, while figures 15(*c*) and (*d*) indicate a modest decrease in core carbon concentration and radiation. Importantly, figures 15(*e*) and (*f*) show that the peak heat flux is reduced by a factor of 5 prior to the onset

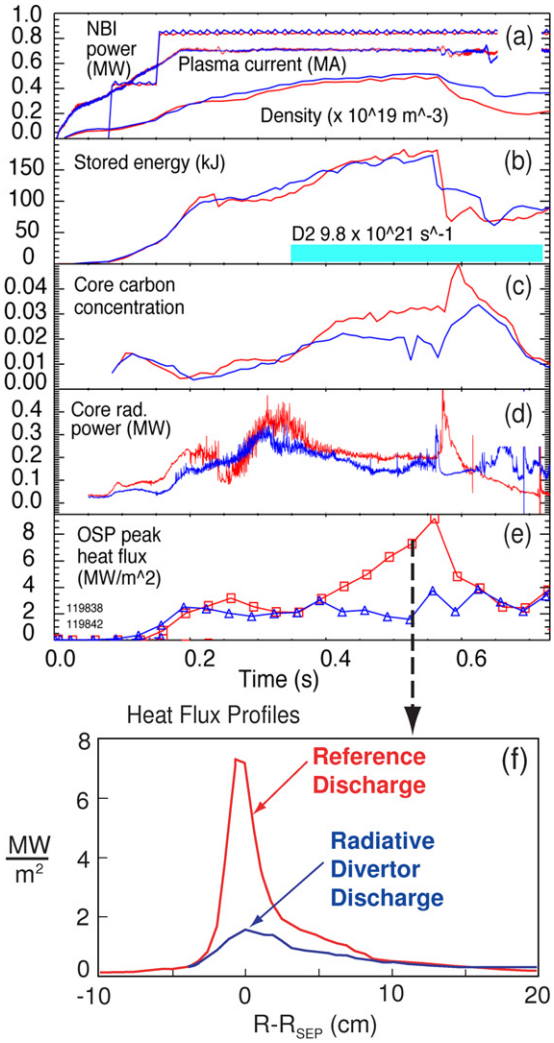

Figure 15. Time evolution of (*a*) I_P, line-average density, and NBI heating power, (*b*) plasma stored energy, (*c*) core carbon concentration, (*d*) core radiated power, (*e*) peak divertor heat flux and (*f*) radial profile of divertor heat flux for reference and radiative divertor discharges.

of β-limiting MHD present in both the reference and radiative divertor discharge. Recent experiments also indicate that the peak divertor heat flux is a strong function of heating power and plasma current [45].

Even with the divertor heat flux reduction techniques described above, solid plasma facing components (PFCs) may be incapable of handling the very high peak divertor heat fluxes projected for future fusion power reactors such as ARIES-AT [46] (14 MW m^{-2}) or ARIES-ST [47] (33 MW m^{-2}). Liquid metal divertors offer a possible solution to this heat flux problem, and following the success of liquid lithium for particle pumping [48] and peak heat flux mitigation in CDX-U, the NSTX has also been pursuing a staged approach to lithium PFC development. Following success in demonstrating particle pumping with lithium pellet conditioning, the NSTX has used a lithium evaporator to achieve more rapid coatings of PFCs [49]. As shown on the left-hand side of figure 16, the NSTX Li-evaporator was designed to provide broad coverage of the lower centrestack and divertor region. H-modes are observed to be the most challenging plasma scenarios to

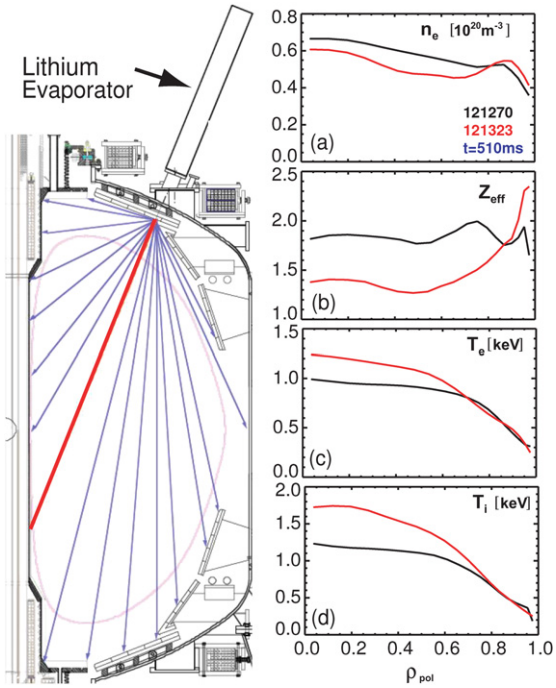

Figure 16. Comparisons of (*a*) n_e, (*b*) Z_{eff}, (*c*) T_e and (*d*) T_i before (black) and after (red) lithium evaporation conditioning.

achieve density control using Li-evaporation. While strong pumping is observed early in such discharges, the rise in density rate later in the discharge is usually similar to that observed without Li-evaporation. Figure 16(*a*) shows the modest 10–15% core density decrease achieved after lithium coating late in H-mode discharges. However, evaporated lithium has been observed to have a more pronounced effect on other discharge parameters. Figure 16(*b*) shows that Li-evaporation reduces the plasma Z_{eff} by up to 35%, and as evident in figures 16(*c*) and (*d*), increases the electron and ion temperatures by up to 25% and 40%, respectively. Lithium is observed to improve the H-mode confinement enhancement factor relative to ITER98PB(y,2) from $HH = 1.08$ to 1.28. Such thermal confinement enhancements improve the prospects for achieving fully NI scenarios discussed in section 1. Development of a liquid lithium divertor target is being considered for the NSTX to provide both enhanced particle pumping and initial studies of high-heat-flux handling capability.

6. Solenoid-free current formation and ramp-up

To minimize the radial build and maintain the low aspect ratio in future reactors, elimination of the central solenoid is highly desirable. Such elimination is only possible with alternative means of plasma current formation and ramp-up. Plasma current formation using coaxial helicity injection (CHI) has recently demonstrated record values of closed-flux plasma current up to 160 kA [50, 51]. Consistent with flux closure, figure 17(*a*) shows that the plasma current which persists after the CHI injector current (I_{INJ}) reaches zero at $t = 9$ ms, and further analysis indicates the plasma current decays inductively with a decay-rate consistent with the measured $T_e = 20$–30 eV. The central electron density during the early I_P decay

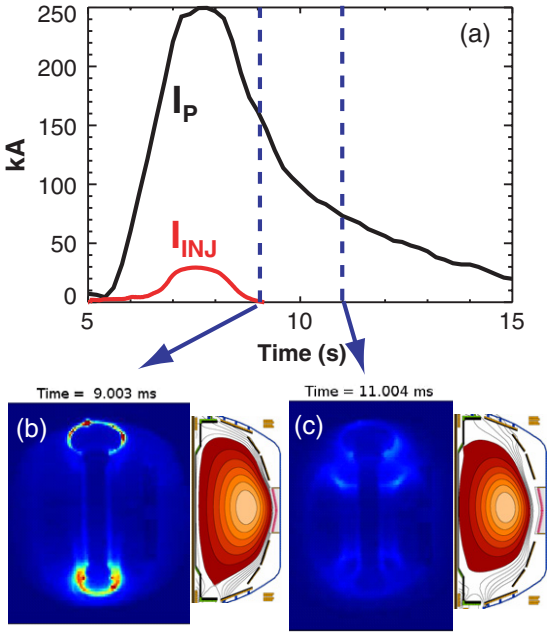

Figure 17. (*a*) Plasma and injector currents versus time and fast-camera images and flux-surface reconstructions at (*b*) peak closed-flux I_P and (*c*) during I_P decay.

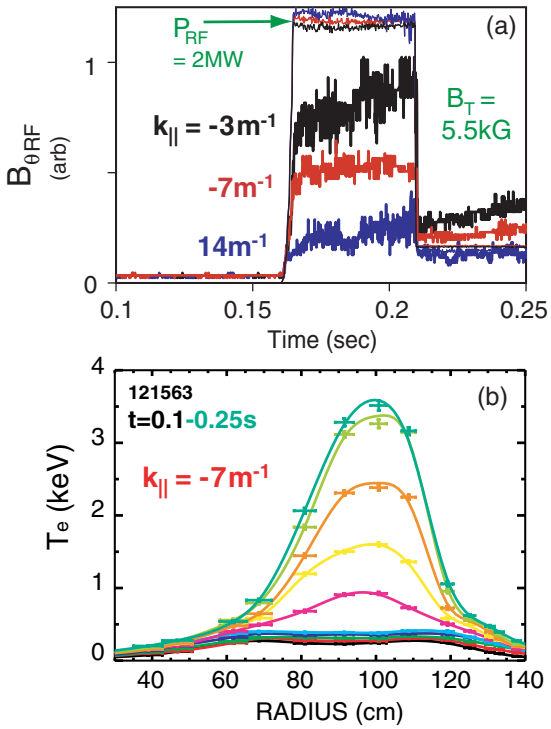

Figure 18. (*a*) Far-field HHFW B_θ amplitude versus launched $k_{||}$ and (*b*) $T_e(t, R)$ for an $I_P = 700$ kA $B_T = 5.5$ kG target plasma heated with 2 MW of HHFW.

phase is $n_e = 1 - 4 \times 10^{18}$ m^{-3}, so the electron collisionality $\nu_{*e} = 2$–10. Resistive losses assuming Spitzer resistivity can account for much of the inductive input power, and this finding may help explain why impurity burn-through is not achieved and T_e remains relatively low. As seen in figure 17(*b*), after the injector current has been turned off and the open-field-line currents have decayed away, fast-camera images exhibit light emission consistent with the reconstructed lower single null separatrix geometry. Later in the discharge, both camera images and reconstructions show the plasma has detached from the lower divertor coil as evident in figure 17(*c*).

A key research goal is to extend CHI plasmas to higher I_P and T_e. Recent electron bernstein wave (EBW) emission measurements [17] indicate that EBW heating and current drive could ultimately contribute to this goal. HHFW heating has already demonstrated the ability of heating $I_P = 250$ kA ohmic plasmas from 200 eV to 1.6 keV in H-mode with f_{BS} of up to 80% [22]. Thus, if higher-T_e CHI target plasmas could be produced, HHFW should be capable of further heating and increasing I_P through BS and FW current overdrive. However, parasitic losses from parametric decay instabilities (PDI) [52] have previously been shown to increase in severity at the lower $k_{||}$ needed for HHFW current drive. More recently, as shown in figure 18(*a*), wave-fields far from the antenna have been measured to increase as $k_{||}$ is lowered. These measurements are consistent with enhanced surface wave excitation and losses at the very low cutoff density associated with low $k_{||}$. Both PDI and surface-waves are expected to be reduced at higher TF and/or higher $k_{||}$. Taking advantage of this new understanding and operating at the highest allowable toroidal field = 0.55 T, figure 18(*b*) shows near record T_e values approaching 4 keV achieved with current-drive phasing. Previously, such high T_e was only achievable with heating phasing ($k_{||} = 14$m^{-1}) [53]. Importantly, these high temperatures obtained with current-drive phasing are achieved with a target plasma temperature of only 200 eV, and it should be possible to heat even lower target plasma temperatures with heating phasing. Thus, the above results improve the prospects for utilizing wave heating and current ramp-up of CHI target plasmas to initiate high performance ST plasmas.

7. Summary

The NSTX has made significant progress in achieving and understanding sustained high-performance operation above the ideal no-wall stability limit with high NI current fraction and H-mode energy confinement ($HH_{98IPB(y,2)} \geqslant 1$). The NSTX research is contributing to an improved understanding of energy confinement scaling and the underlying causes of anomalous energy transport, the effect of multiple fast-ion instabilities on energetic particle confinement, novel methods for particle and divertor heat flux control and solenoid-free plasma current formation and ramp-up physics. These results strengthen the scientific foundation for high performance operation in both ITER and future ST devices.

Acknowledgments

The author of this paper is supported by the US-DOE contract DE-AC02-76CH03073.

References

[1] Ono M. *et al* 2000 *Nucl. Fusion* **40** 557
[2] Kaye S.M. *et al* 2005 *Nucl. Fusion* **45** S168

[3] Peng Y.-K.M. and Strickler D.J. 1986 *Nucl. Fusion* **26** 769
[4] Bell M.G. *et al* 2006 *Nucl. Fusion* **46** S565
[5] Gates D.A. *et al* 2006 *Phys. Plasmas* **13** 056122
[6] Levinton F. 2004 *Bull. Am. Phys. Soc.* **49** 221
[7] Zhu W. *et al* 2006 *Phys. Rev. Lett.* **96** 225002
[8] Sabbagh S.A. *et al* 2006 *Phys. Rev. Lett.* **97** 045004
[9] Mikkelsen D.R. 1989 *Phys. Fluids* B **1** 333
[10] Peng Y.-K.M. *et al* 2005 *Plasma Phys. Control. Fusion* **47** B263
[11] Menard J.E. *et al* 2006 *Phys. Rev. Lett.* **97** 095002
[12] Gates D.A. *et al* 2006 *Nucl. Fusion* **46** 17
[13] Maingi R. *et al* 2006 *Phys. Plasmas* **13** 092510
[14] Menard J.E. *et al* 2004 *Phys. Plasmas* **11** 639
[15] Sontag A.C. *et al* 2005 *Phys. Plasmas* **12** 056112
[16] Sabbagh S.A. *et al* 2006 *Nucl. Fusion* **46** 635
[17] Gates D.A. *et al* 2006 *Proc. 21st Int. Conf. on Fusion Energy 2006 (Chengdu)* (Vienna: IAEA) Paper EX/P1-3 CD-ROM and http://www-naweb.iaea.org/napc/physics/FEC/FEC2006/html/index.htm
[18] Luce T.C. and DIII-D Team 2005 *Nucl. Fusion* **45** S86
[19] Sauter O., Angioni C. and Lin-Liu Y.R. 1999 *Phys. Plasmas* **6** 2834
[20] Goldston R.J., Mccune D.C. and Towner H.H. 1981 *J. Comput. Phys.* **43** 61
[21] Medley S.S. *et al* 2006 *Proc. 21st Int. Conf. on Fusion Energy 2006 (Chengdu)* (Vienna: IAEA) Paper EX/P6-13 CD-ROM and http://www-naweb.iaea.org/napc/physics/FEC/FEC2006/html/index.htm
[22] Kessel C.E. *et al* 2006 *Phys. Plasmas* **13** 056108
[23] La Haye R.J. *et al* 1992 *Phys. Fluids* B **4** 2098
[24] Buttery R.J., De'benedetti M., Hender T.C. and Tubbing B.J.D. 2000 *Nucl. Fusion* **40** 807
[25] Lazzaro E. *et al* 2002 *Phys. Plasmas* **9** 3906
[26] Garofalo A.M. *et al* 2002 *Phys. Rev. Lett.* **89** 235001
[27] Reimerdes H. *et al* 2004 *Phys. Rev. Lett.* **93** 135002
[28] Sontag A.C. *et al* 2006 *Proc. 21st Int. Conf. on Fusion Energy 2006 (Chengdu)* (Vienna: IAEA) Paper EX/7-2Rb CD-ROM and http://www-naweb.iaea.org/napc/physics/FEC/FEC2006/html/index.htm
[29] Kaye S.M. *et al* 2006 *Nucl. Fusion* **46** 848
[30] Kaye S.M. *et al* 2006 *Proc. 21st Int. Conf. on Fusion Energy 2006 (Chengdu)* (Vienna: IAEA) Paper EX/8-6 CD-ROM and http://www-naweb.iaea.org/napc/physics/FEC/FEC2006/html/index.htm
[31] Kotschenreuther M., Rewoldt G. and Tang W.M. 1995 *Comput. Phys. Commun.* **88** 128
[32] Stutman D. *et al* 2006 *Proc. 33rd EPS (Rome)* Paper P5.120
[33] Fredrickson E.D. *et al* 2006 *Phys. Plasmas* **13** 056109
[34] Crocker N.A. *et al* 2006 *Phys. Rev. Lett.* **97** 045002
[35] Evans T.E. *et al* 2004 *Phys. Rev. Lett.* **92** 235003
[36] Yan L., Evans T.E., Kaye S.M. and Maingi R. 2006 *Nucl. Fusion* **46** 858
[37] Maingi R. *et al* 2005 *Nucl. Fusion* **45** 264
[38] Maingi R. *et al* 2005 *Nucl. Fusion* **45** 1066
[39] Maingi R. *et al* 2006 *Proc. 21st Int. Conf. on Fusion Energy 2006 (Chengdu)* (Vienna: IAEA) Paper IT/P1-12 CD-ROM and http://www-naweb.iaea.org/napc/physics/FEC/FEC2006/html/index.htm
[40] Myra J.R., Russell D.A. and Dippolito D.A. 2006 *Phys. Plasmas* **13** 112502
[41] Myra J.R. *et al* 2006 *Phys. Plasmas* **13** 092509
[42] Boedo J.A. *et al* 2006 *Proc. 21st Int. Conf. on Fusion Energy 2006 (Chengdu)* (Vienna: IAEA) Paper EX/P4-2 CD-ROM and http://www-naweb.iaea.org/napc/physics/FEC/FEC2006/html/index.htm
[43] Soukhanovskii V.A. *et al* 2006 *Proc. 21st Int. Conf. on Fusion Energy 2006 (Chengdu)* (Vienna: IAEA) Paper EX/P4-28 CD-ROM and http://www-naweb.iaea.org/napc/physics/FEC/FEC2006/html/index.htm
[44] Soukhanovskii V.A. *et al* 2005 *J. Nucl. Mater.* **337–339** 475
[45] Maingi R. *et al* 2007 Divertor heat flux scaling with heating power and plasma current in H-mode discharges in the national spherical torus experiment *J. Nucl. Mater.* at press
[46] Najmabadi F. *et al* 2006 *Fusion Eng. Des.* **80** 3
[47] Jardin S.C. *et al* 2003 *Fusion Eng. Des.* **65** 165
[48] Majeski R. *et al* 2006 *Phys. Rev. Lett.* **97** 075002
[49] Majeski R. *et al* 2006 *Proc. 21st Int. Conf. on Fusion Energy 2006 (Chengdu)* (Vienna: IAEA) Paper EX/P4-23 CD-ROM and http://www-naweb.iaea.org/napc/physics/FEC/FEC2006/html/index.htm
[50] Raman R. *et al* 2006 *Phys. Rev. Lett.* **97** 175002
[51] Raman R. *et al* 2006 *Proc. 21st Int. Conf. on Fusion Energy 2006 (Chengdu)* (Vienna: IAEA) Paper EX/P8-16 CD-ROM and http://www-naweb.iaea.org/napc/physics/FEC/FEC2006/html/index.htm
[52] Biewer T.M. *et al* 2005 *Phys. Plasmas* **12** 056108
[53] Leblanc B.P. *et al* 2004 *Nucl. Fusion* **44** 513